Draft version February 7, 2020
Typeset using LaTeX **twocolumn** style in AASTeX62

Two intermediate-mass brown dwarfs from the TESS mission

Theron W. Carmichael,[1,2,3] Samuel N. Quinn,[2] Alexander J. Mustill,[4] Chelsea Huang,[5] George Zhou,[2] Carina M. Persson,[6] Louise D. Nielsen,[7] Karen A. Collins,[2] Carl Ziegler,[8] Kevin I. Collins,[9] Joseph E. Rodriguez,[2] Avi Shporer,[5] Rafael Brahm,[10,11,12] Andrew W. Mann,[13] Francois Bouchy,[7] Malcolm Fridlund,[6,14] Keivan G. Stassun,[15,16] Coel Hellier,[17] Julia V. Seidel,[7] Manu Stalport,[7] Stephane Udry,[7] Francesco Pepe,[7] Michael Ireland,[18] Maruša Žerjal,[18] César Briceño,[19] Nicholas Law,[13] Andrés Jordán,[20,12] Néstor Espinoza,[21] Thomas Henning,[22] Paula Sarkis,[22] and David W. Latham[2]

[1]Harvard University, Cambridge, MA 02138
[2]Center for Astrophysics | Harvard & Smithsonian, 60 Garden Street, Cambridge, MA 02138, USA
[3]National Science Foundation Graduate Research Fellow
[4]Lund Observatory, Department of Astronomy and Theoretical Physics, Lund University, Box 43, SE-221 00 Lund, Sweden
[5]Department of Physics, and Kavli Institute for Astrophysics and Space Research, Massachusetts Institute of Technology, Cambridge, MA 02139, USA
[6]Chalmers University of Technology, Department of Space, Earth and Environment, Onsala Space Observatory, SE-439 92 Onsala, Sweden
[7]Geneva Observatory, University of Geneva, Chemin des Mailettes 51, 1290 Versoix, Switzerland
[8]Dunlap Institute for Astronomy and Astrophysics, University of Toronto, 50 St. George Street, Toronto, Ontario M5S 3H4, Canada
[9]George Mason University, 4400 University Drive, Fairfax, VA, 22030 USA
[10]Center of Astro-Engineering UC, Pontificia Universidad Católica de Chile, Av. Vicuña Mackenna 4860, 7820436 Macul, Santiago, Chile
[11]Instituto de Astrofísica, Pontificia Universidad Católica de Chile, Av. Vicuña Mackenna 4860, Macul, Santiago, Chile
[12]Millennium Institute for Astrophysics, Chile
[13]Department of Physics and Astronomy, The University of North Carolina at Chapel Hill, Chapel Hill, NC 27599-3255, USA
[14]Leiden Observatory, University of Leiden, PO Box 9513, 2300 RA, Leiden, The Netherlands
[15]Vanderbilt University, Department of Physics & Astronomy, 6301 Stevenson Center Ln., Nashville, TN 37235, USA
[16]Fisk University, Department of Physics, 1000 18th Ave. N., Nashville, TN 37208, USA
[17]Astrophysics Group, Keele University, Staffordshire, ST5 5BG, UK
[18]Research School of Astronomy and Astrophysics, The Australian National University, ACT, 2611
[19]Cerro Tololo Inter-American Observatory, Casilla 603, La Serena, Chile
[20]Facultad de Ingeniera y Ciencias, Universidad Adolfo Ibáñez, Av. Diagonal las Torres 2640, Peñalolén, Santiago, Chile
[21]Space Telescope Science Institute, 3700 San Martin Drive, Baltimore, MD 21218, USA
[22]Max-Planck-Institut für Astronomie, Königstuhl 17, Heidelberg 69117, Germany

ABSTRACT

We report the discovery of two intermediate-mass brown dwarfs (BDs), TOI-569b and TOI-1406b, from NASA's Transiting Exoplanet Survey Satellite mission. TOI-569b has an orbital period of $P = 6.55604 \pm 0.00016$ days, a mass of $M_b = 63.8 \pm 1.0\,\mathrm{M_J}$, and a radius of $R_b = 0.75 \pm 0.02\,\mathrm{R_J}$. Its host star, TOI-569, has a mass of $M_\star = 1.21 \pm 0.03\,\mathrm{M_\odot}$, a radius of $R_\star = 1.48 \pm 0.03\,\mathrm{R_\odot}$, and an effective temperature of $T_{\rm eff} = 5705 \pm 76$K. TOI-1406b has an orbital period of $P = 10.57415 \pm 0.00063$ days, a mass of $M_b = 46.0 \pm 2.7\,\mathrm{M_J}$, and a radius of $R_b = 0.86 \pm 0.03\,\mathrm{R_J}$. The host star for this BD has a mass of $M_\star = 1.18 \pm 0.09\,\mathrm{M_\odot}$, a radius of $R_\star = 1.35 \pm 0.03\,\mathrm{R_\odot}$, and an effective temperature of $T_{\rm eff} = 6290 \pm 100$K. Both BDs are in circular orbits around their host stars and join an increasing number of known transiting intermediate-mass BDs. TOI-569 is one of two slightly evolved stars known to host a transiting BD (the other being KOI-415). TOI-1406b is one of three known transiting BDs to occupy the mass range of 40-50 $\mathrm{M_J}$ and one of two to have a circular orbit at a period near 10 days (with the first being KOI-205b). Based on the relatively long circularization timescales for both BDs, we believe that they must have formed in nearly circular orbits and migrated inward to their present orbital configurations.

Keywords: brown dwarfs – techniques: photometric – techniques: radial velocities – techniques: spectroscopic

1. INTRODUCTION

The Transiting Exoplanet Survey Satellite (TESS) mission has aided in the discovery and characterization

of two new transiting brown dwarfs (BDs) in the past year (Jackman et al. 2019; Subjak et al. 2019). BDs are generally defined as objects with masses between 13 and 80 Jupiter masses (M_J) and, for those that orbit main-sequence stars, are typically observed to be 0.7 to 1.4 Jupiter radii (R_J) in size (Csizmadia & CoRot Team 2016; Carmichael et al. 2019). The mass limits correspond to the threshold required to fuse deuterium in the core of the BD (roughly $13\,M_J$, separating planets from BDs) and the threshold to fuse hydrogen in the core ($80\,M_J$, separating BDs from stars). The mass and radius of a BD are measured though a combination of observational techniques, with two of the most important being transit photometry and radial velocity (RV) measurements. The transit method is best utilized for BDs in relatively short orbital periods (on order of 10 days or less to detect multiple transits), which is why the TESS mission has been particularly useful in making the initial detection of the transiting BD that Subjak et al. (2019) recently discovered. The transit light curves from TESS are taken over roughly 28 consecutive days per sector (or up to one year for overlapping sectors), with occasional gaps in coverage due to instrumental systematics. These light curves give estimates of the radius of the candidate companions to stars. This informs us on whether or not a candidate companion is within the typical range of radii expected for a BD orbiting a main-sequence star.

Follow up spectra are then taken to construct a series of RV measurements to determine an orbit and measure a mass to verify whether or not the candidate companion is in the BD mass range. This is an important step as objects ranging from roughly $1\,M_J$ to $100\,M_J$ may have the same radius ($\sim 1\,R_J$), so the only way to distinguish them is through measuring the mass. We are particularly fortunate at the present time to be able to utilize the parallax measurements from *Gaia* DR2 to derive precise stellar radii for the stars hosting transiting BDs, which directly impacts how well we measure the companion radius.

Though this process of detecting and characterizing transiting BDs is well-established and fairly accessible given the precision of modern spectrographs, we only know of 23 transiting BDs (e.g. Siverd et al. 2012; Bonomo et al. 2015; Zhou et al. 2019; Carmichael et al. 2019; Subjak et al. 2019). When compared to the number of known transiting hot Jupiters and eclipsing low-mass stellar companions in comparable orbital periods (i.e. less than 100 days), it is clear that there is a lack of BDs; this is the so-called "brown dwarf desert" (Marcy & Butler 2000).

Despite not fully understanding the origins of this desert, we may still strive to understand the nature of the population of the objects in the $13\,M_J$ to $80\,M_J$ mass range. Ma & Ge (2014) contribute to this pursuit of knowledge by proposing the existence of a gap within the the brown dwarf desert centered on $42.5\,M_J$, implying that two sub-populations of BDs exist above and below this mass. Another study by Persson et al. (2019) implies that the mass range of giant planets spans 0.3-73 M_J based on a mass-density relation. These differences in ideas highlight the importance of the detection and characterization of new transiting BDs. With a transit, orbital solution, and well-determined stellar radius, we have all the components required to precisely measure the mass and radius of a transiting BD. So, each newly discovered transiting BD will add another member to this scarcely populated region of objects.

The mass and radius of a transiting BD are useful in understanding how these substellar objects evolve when compared to evolutionary models that consider the presence of a main sequence host star (e.g. Baraffe et al. 2003). Since a BD may only fuse deuterium and not hydrogen, it lacks the energy source needed to stave off gravitational contraction on long timescales as effectively as stars do, so the BD's radius will shrink as it ages. Thus, the age also becomes an important property of a transiting BD, and this is something we may explore with substellar evolutionary models.

Age is a particularly difficult parameter to measure for stars and BDs. This makes it all the more important that we have some reasonable estimate of the age as the age of a transiting BD may be compared to its circularization timescale for the system it is in. These timescales, though not well-understand for short-period, transiting BDs, are used to understand a BDs formation and past orbital evolution.

One method to measuring the age of a transiting BD is done via its association with a star cluster or stream. There are only 3 transiting BD systems that are in clusters or stellar associations (Nowak et al. 2017; Gillen et al. 2017; David et al. 2019), so in general, this population is lacking in systems with directly measured ages. If we are not fortunate enough to have a directly measurable age, then we rely on stellar isochrone models in combination with parallax measurements form the *Gaia* mission and measurements of the spectral energy distribution (SED) of the host star. This method is limited by how well the metallicity and effective temperature of the star is measured.

Here we report the discovery and characterization of TOI-569b and TOI-1406b. TOI-569b orbits a recently evolved star in a circular orbit. TOI-1406b orbits an

F-type star, joining 7 other transiting BDs that orbit F-type stars, and is also in a circular orbit. Section 2 gives details on the light curves and spectra that were obtained for this study with additional attention given to the determination of the orbital period of TOI-569b, which was initially reported incorrectly due to gaps in the TESS data. Section 3 describes the analysis techniques used to derive the host star and BD properties. Section 4 contains discussion of the implications of these new discoveries in the BD mass-radius diagram and some discussion on the circularization timescales for each system.

2. OBSERVATIONS

2.1. *TESS and ground-based light curves*

The light curves of TOI-569 come from the TESS mission in sectors 7 and 8, and the Las Cumbres Observatory (LCO). For the TESS light curve for TOI-569, we use the Pre-search Data Conditioning Simple Aperture Photometry flux (PDCSAP; Stumpe et al. 2014; Smith et al. 2012) from the Mikulski Archive for Space Telescopes (MAST)[1]. The PDCSAP light curve has systematic effects removed and with this, we then normalize light curve with the `lightkurve` package in Python (the Lightkurve Collaboration et al. 2018). The light curves used for TOI-1406 come from the full-frame images (30 minute cadence) from the TESS mission in sectors 4, 5, and 6. We use the `lightkurve` package to extract and normalize the light curve of TOI-1406.

We observed an ingress of TOI-569 continuously for 140 minutes on April 15, 2019 using 15 s exposures and a z-short band filter from the LCO (Brown et al. 2013) 1.0 m node at Cerro Tololo Inter-American Observatory. We used the `TESS Transit Finder`, which is a customized version of the `Tapir` software package (Jensen 2013), to schedule our transit observations. The 4096×4096 LCO SINISTRO cameras have an image scale of $0.389''$ per pixel, resulting in a $26' \times 26'$ field of view. The images were calibrated by the standard LCO BANZAI pipeline, and photometric data were extracted with the `AstroImageJ` software package (Collins et al. 2017) using a circular aperture with radius $5.8''$. The images have typical stellar point-spread-functions with a half-width-half-maximum of $1''$. We detect a ~ 3000 ppm ingress on target with apertures as small as $2''$. Systematic effects start to dominate the light curve for smaller apertures. Thus, we confirm that the source of the TESS detection is within $3''$ of the target star location and that the transit depth from the LCO partial transit is consistent with the TESS depth for all aperture radii we checked down to $2''$. We do not take any ground-based photometric followup of TOI-1406.

[1] https://mast.stsci.edu/portal/Mashup/Clients/Mast/Portal.html

Table 1. Coordinates and magnitudes for TOI-569 and TOI-1406.

	Description	TOI-569	TOI-1406	Source
α_{J2000}	Equatorial	07 40 24.67	05 28 30.71	1
δ_{J2000}	coordinates	-42 09 16.79	-48 24 32.64	1
T	TESS T	9.473 ± 0.006	11.427 ± 0.006	2
G	Gaia G	9.936 ± 0.001	11.759 ± 0.001	1
B_T ...	Tycho B_T ..	11.036 ± 0.048	13.352 ± 0.359	3
V_T	Tycho V_T ...	10.173 ± 0.032	12.074 ± 0.195	3
J	2MASS J ...	8.829 ± 0.020	10.929 ± 0.020	4
H	2MASS H ..	8.575 ± 0.060	10.787 ± 0.030	4
K_S ...	2MASS K_S .	8.444 ± 0.020	10.675 ± 0.020	4
WISE1	WISE 3.4μm	8.419 ± 0.023	10.649 ± 0.023	5
WISE2	WISE 4.6μm	8.467 ± 0.020	10.692 ± 0.021	5
WISE3	WISE 12μm	8.414 ± 0.021	10.651 ± 0.062	5
WISE4	WISE 22μm	8.180 ± 0.188	-	5

NOTE—References: 1 - Lindegren et al. (2018), 2 - Stassun et al. (2018b), 3 - Høg et al. (2000), 4 - Cutri et al. (2003), 5 - Cutri & et al. (2013)

2.1.1. *Light curve modulation and the orbital period of the TOI-569 system*

Previous to the transit detections of TOI-569b from TESS, the Wide Angle Search for Planets (WASP) found a 13-day modulation in the light curve of TOI-569. The phased light curve for WASP is shown in Figure 2. The WASP data were taken during the 2011 to 2012 seasons with a total of 150 days of coverage. The transits of TOI-569b are too shallow to be detected in the WASP light curve, but they can be seen in the TESS light curve in the top panel of Figure 2. The WASP and TESS light curves show a similar but not exactly equal modulation. The period peaks and dips in both light curves are likely from brightness variations due to star spots, which may vary in the total brightness difference over time (especially the 150-day WASP observing period). The unevenness in the peaks in the TESS light curves are likely from two different star spot configurations on different areas on the surface of the star.

The gaps in the TESS light curve occur during every other transit of TOI-569b in the sectors the host star was observed. This means that the initial orbital period was reported to be 13.11 days (twice the true orbital period of 6.56 days). We discovered that this was the case as the orbital solution developed with RV follow

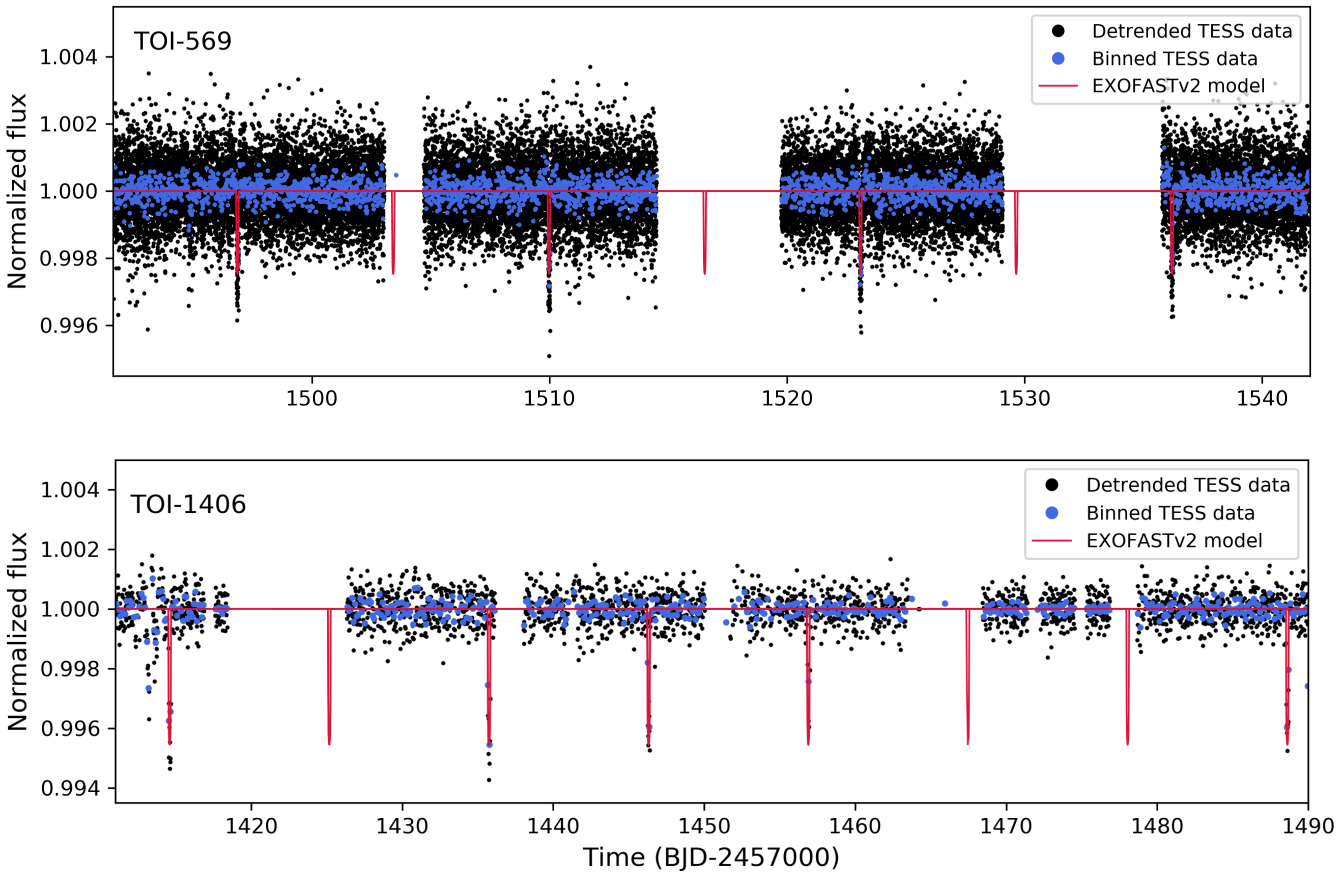

Figure 1. *Top*: Detrended TESS light curve of TOI-569. The star was observed at 2 minutes cadence in TESS sectors 7 and 8. This star also exhibits 1-3% periodic variations in flux likely due to star spots; these effects have been removed for the transit analysis. *Bottom*: Detrended TESS light curve of TOI-1406 obtained from the full-frame images at 30 minute cadence from TESS sectors 4, 5, and 6.

up using the instruments described in later sections. It seems coincidental that this erroneous orbital period of 13.11 days is nearly equal to the 13-day modulation in the WASP light curve. This would make the BD appear to have a synchronized orbit with the rotation rate of the star, but this is not the case upon a more thorough investigation that accounts for the orbital solution derived from RVs.

2.2. *High resolution imaging and contaminating sources*

For TOI-569, we use SOAR speckle imaging to verify that there are no objects within the TESS aperture that would significantly contaminate the transit and RV signals we observe. Nearby stars which fall within the same TESS image profile as the target can cause photometric contamination or be the source of an astrophysical false positive, such as a background or nearby eclipsing binary star. We searched for nearby sources to TOI-569 with SOAR speckle imaging (Tokovinin 2018) on May 18, 2019, observing in a similar visible bandpass as TESS (the Cousins-I band). Further details of the observations are available in Ziegler et al. (2019). We detect no nearby stars within 3″ of TOI-569. The 5-σ detection sensitivity and the speckle auto-correlation function from the SOAR observation are plotted in Figure 3. We also use data from *Gaia* DR2 to confirm this, finding that no stars brighter than G=17.0 are within 25″ and only two stars with G=13.7 and G=14.9 are approximately 26″ from TOI-569, which has a brightness of G=9.9 (Table 2). These other fainter stars also do not share the same proper motion as TOI-569, which further indicates that they are not associated with TOI-569 and are more distant background stars (Gaia Collaboration et al. 2018).

We do not have any high resolution imaging for TOI-1406, but using *Gaia* DR2 data (Gaia Collaboration et al. 2018), we find only 3 other stars within 30″ of TOI-1406. The brightest of these other stars has a magnitude of G=15.8 and is 19″ from TOI-1406, which has a magnitude of G=11.8. We also find that none of these

Table 2. Nearby sources from *Gaia* DR2 data. This table list sources within 30″ of each star (TOI-569 and TOI-1406) that are $G < 16$ in magnitude. Listing sources fainter than this results in too many items to reasonably list here. The parallaxes (π) and proper motions (μ_α, μ_δ) of the nearby stars indicate that none are associated with TOI-569 or TOI-1406.

Gaia DR2 ID	α_{J2000}	δJ2000	π (mas)	μ_α (mas/yr)	μ_δ (mas/yr)	G (mag)
5535473358555685760 (TOI-569)	07 40 24.67	-42 09 16.79	6.3723 ± 0.0306	6.317 ± 0.053	-3.068 ± 0.048	9.94
5535473392915426304	07 40 26.44	-42 09 00.02	0.0899 ± 0.0193	-1.790 ± 0.035	2.832 ± 0.030	13.69
5535473358555686656	07 40 23.61	-42 09 39.57	0.8838 ± 0.0275	12.130 ± 0.047	-13.344 ± 0.041	14.88
5535473358556195840	07 40 23.25	-42 09 38.38	0.1963 ± 0.0414	-4.600 ± 0.072	5.585 ± 0.060	15.64
4797030079342886784 (TOI-1406)	05 28 30.71	-48 24 32.64	2.3855 ± 0.0291	0.889 ± 0.057	-21.885 ± 0.066	11.76
4797030079342886656	05 28 29.07	-48 24 41.93	1.1846 ± 0.0396	1.222 ± 0.073	-1.752 ± 0.093	15.78

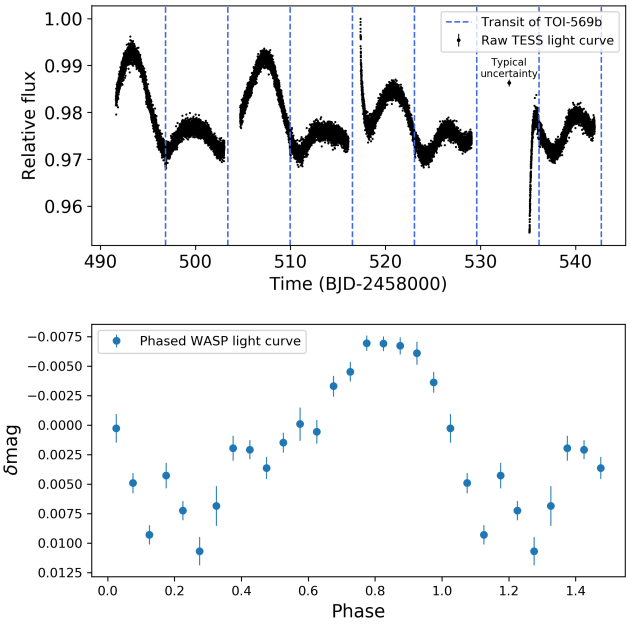

Figure 2. *Top*: Offset-normalized raw TESS light curve from sectors 7 and 8 of TOI-569. The offset between each sector is removed using `lightkurve`, but no other systematic effects are removed since the focus of this figure is to show the missed transits of TOI-569b and provide context for the flux variability of the host star. The rapid ramp down at 515 days and ramp up at 535 days are instrumental systematics from the spacecraft. The blue lines show the transits of TOI-569b. *Bottom*: WASP light curve of TOI-569 phase folded at 13.03 days from observations taken over a time of 150 days.

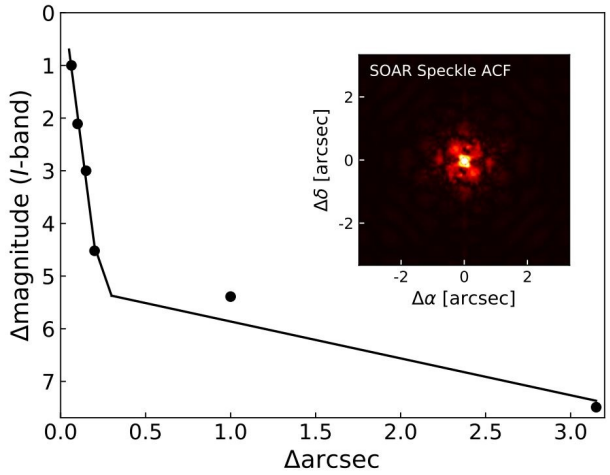

Figure 3. The 5-σ sensitivity limits and auto-correlation functions of the SOAR speckle observations of TOI-569. The black circles are measured data points and the lines are fits in two different separation regimes. In general, the sensitivity of speckle imaging to companions rises sharply from the diffraction limit to a "knee" at a separation of $0.15 - 0.2''$, where it then continues to slowly increase out to $1.5''$, beyond which the speckle patterns begin to become de-correlated. No nearby contaminating sources are detected within $3''$.

other stars share the same proper motion as TOI-1406 from the *Gaia* DR2 data (Table 2).

2.3. *CHIRON spectra*

To characterize the RVs and stellar atmospheric parameters of TOI-569 and TOI-1406, we obtained a series of spectroscopic observations using the CHIRON spectrograph on the 1.5 m SMARTS telescopes, located at Cerro Tololo Inter-American Observatory, Chile. CHIRON is a high resolution echelle spectrograph that is fed via an image slicer and a fiber bundle. CHIRON achieves a spectral resolving power of $\lambda/\Delta\lambda \equiv R \sim 80,000$ over the wavelength region 4100 to 8700 Å. The wavelength calibration is obtained via Thorium-Argon hollow-cathode lamp exposures that bracket each stellar spectrum.

To derive the stellar RVs, we performed a least-squares deconvolution (Donati et al. 1997) between the observed spectra and a non-rotating synthetic template generated via ATLAS9 atmospheric models (Castelli & Kurucz 2004) at the stellar atmospheric parameters of each target. We then model the stellar line profiles derived from the least-squares deconvolution via an analytic ro-

Table 3. Relative radial velocities of TOI-569 from CHIRON, CORALIE, and FEROS and of TOI-1406 from CHIRON and ANU.

$BJD_{TDB} - 2450000$	RV (m/s)	σ_{RV} (m/s)	Instrument	Target
8594.61690	75132.3	16.6	CHIRON	TOI-569
8606.50771	77754.5	20.7	CHIRON	TOI-569
8596.60327	66265.0	18.9	CHIRON	TOI-569
8595.59076	69864.3	16.4	CHIRON	TOI-569
8607.53323	75982.6	17.8	CHIRON	TOI-569
8611.59733	71966.8	24.9	CHIRON	TOI-569
8612.57581	76679.3	30.6	CHIRON	TOI-569
8649.44500	66193.1	24.2	CHIRON	TOI-569
8651.48774	74957.8	34.9	CHIRON	TOI-569
8654.46711	70453.9	27.2	CHIRON	TOI-569
8593.58587	79347.5	13.0	CORALIE	TOI-569
8597.47058	68533.2	31.6	CORALIE	TOI-569
8599.52446	78333.6	16.8	CORALIE	TOI-569
8602.58567	69230.9	13.3	CORALIE	TOI-569
8603.46595	67533.0	20.3	CORALIE	TOI-569
8614.49353	75527.3	32.4	CORALIE	TOI-569
8615.48815	70140.4	29.5	CORALIE	TOI-569
8594.49170	77148.3	6.5	FEROS	TOI-569
8595.52217	71681.8	8.4	FEROS	TOI-569
8597.51010	68686.8	6.8	FEROS	TOI-569
8617.52568	70033.1	6.0	FEROS	TOI-569
8540.61381	-13631.0	69.2	CHIRON	TOI-1406
8541.60193	-15950.3	91.8	CHIRON	TOI-1406
8542.56709	-17888.9	45.1	CHIRON	TOI-1406
8544.52353	-19087.2	166.4	CHIRON	TOI-1406
8546.51779	-15936.1	91.8	CHIRON	TOI-1406
8562.57958	-15177.2	126.9	CHIRON	TOI-1406
8566.55925	-18101.1	97.7	CHIRON	TOI-1406
8567.59295	-16029.1	83.6	CHIRON	TOI-1406
8568.54388	-13973.3	124.3	CHIRON	TOI-1406
8569.57364	-12432.3	110.3	CHIRON	TOI-1406
8533.07797	-19568.3	465.0	ANU	TOI-1406
8534.98787	-17679.4	197.8	ANU	TOI-1406
8536.06364	-15764.1	260.2	ANU	TOI-1406
8537.96961	-12090.1	725.7	ANU	TOI-1406
8538.93516	-12135.5	282.9	ANU	TOI-1406
8561.89365	-13798.5	270.0	ANU	TOI-1406

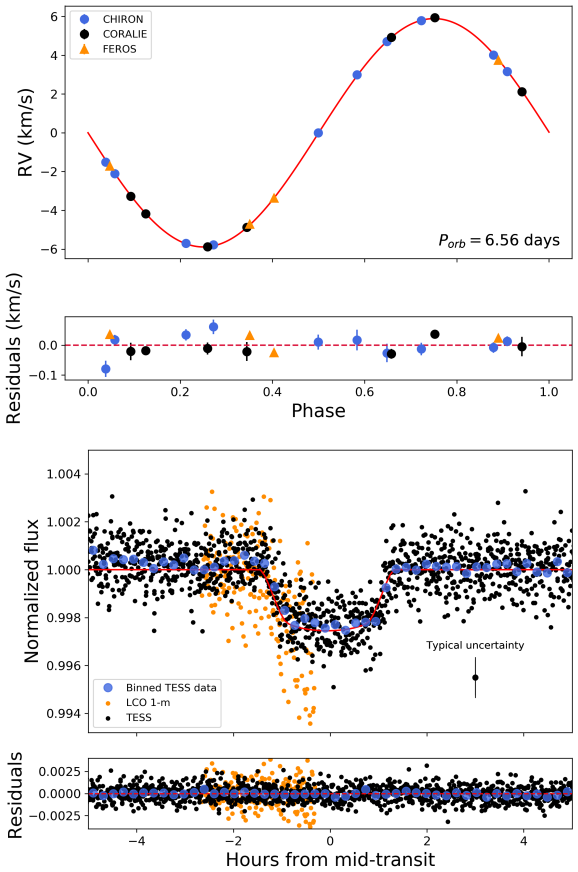

Figure 4. *Top*: Relative radial velocities of TOI-569 with `EXOFASTv2` orbital solution plotted in red. *Bottom*: TESS and LCO light curves with `EXOFASTv2` transit model in red.

tational broadening kernel as per Gray (2005). The derived RVs for TOI-569 and TOI-1406 are listed in Table 3. The stellar parameters derived from the spectra of TOI-569 are $T_{\rm eff} = 5669 \pm 106$K, $\log g = 4.11 \pm 0.18$, [Fe/H] $= 0.23 \pm 0.05$ dex, and $v \sin i = 6.65 \pm 0.10$ km/s.

2.4. *ANU 2.3m echelle spectra*

To help identify TOI-1406b as a BD, we obtained six spectroscopic observations with the echelle spectrograph on the Australian National University (ANU) 2.3 m telescope, located at Siding Spring Observatory, Australia. The ANU 2.3 m echelle is a slit-fed spectrograph that yields a resolving power of $R \sim 23,000$ over the wavelength region of $3700 - 6700$ Å. Wavelength calibration was provided by bracketing Thorium-Argon lamp exposures, and the spectra were reduced as per Zhou et al. (2014). The RVs from each exposure were measured via the least-squares deconvolution technique as described in Section 2.3. To derive $T_{\rm eff}$, $\log g$, and [Fe/H] for TOI-1406, we use `SpecMatch-emp` (Yee et al. 2017), which matches the input spectra to a vast library of stars with well-determined parameters derived with a variety of independent methods, e.g., interferometry, optical and NIR photometry, asteroseismology, and LTE analysis of high-resolution optical spectra. From the ANU spectra and `SpecMatch-emp` we find $T_{\rm eff} = 6283 \pm 110$K, $\log g = 4.13 \pm 0.12$, and [Fe/H] $= -0.09 \pm 0.09$ dex for TOI-1406.

2.5. *CORALIE spectra*

TOI-569 was observed with the CORALIE spectrograph on the Swiss 1.2 m Euler telescope at La Silla Observatories, Chile (Queloz et al. 2001), between April 19 and May 11, 2019. CORALIE has a resolving power of $R \sim 60,000$ and is fed by two fibres; one 2″ on-sky science fibre encompassing the star and another which can either be connected to a Fabry-Pérot etalon for simultaneous wavelength calibration or on-sky for background subtraction of the sky-flux. RVs were computed for each epoch by cross-correlating with a binary G2 mask (Pepe et al. 2002). Bisector-span, full-width half-max. and other line-profile diagnostics were computed as well using the standard CORALIE data reduction software. Initial observations showed a 10.8 km/s RV shift over 3 days, and we subsequently reduced the exposure time from 1200 seconds to 450-600 seconds depending on seeing and airmass. We obtain a precision of 13-32 m/s. The resulting velocities are plotted in Figure 4, and are listed in Table 3.

The CORALIE spectra were shifted to the stellar rest frame and stacked while weighting the contribution from each spectrum with its mean flux to produce a high signal-to-noise spectrum for spectral characterization using `SpecMatch-emp` (Yee et al. 2017). We used the spectral region around the Mgb triplet (5100 − 5340Å) to match our spectrum to the library spectra through χ^2 minimization. A weighted linear combination of the five best matching spectra were used to extract bulk stellar parameters; $T_{\rm eff} = 5481 \pm 110$K, $\log g = 4.08 \pm 0.12$ and [Fe/H] $= 0.41 \pm 0.09$ dex for TOI-569.

2.6. *FEROS spectra*

TOI-569 was observed with the FEROS spectrograph (Kaufer & Pasquini 1998) mounted on the MPG 2.2 m telescope installed at the ESO La Silla Observatory. Four spectra were obtained between April 20 and May 14, 2019. Observations were performed with the simultaneous calibration mode where a second fibre is illuminated with a Thorium-Argon lamp for tracking the instrumental drift in RV during the science exposure. The adopted exposure time was of 400s which produced spectra with a typical signal-to-noise ratio per resolution element of 90. FEROS data was processed with the `ceres` pipeline (Brahm et al. 2017a), which performs the optimal extraction of the raw data, the wavelength calibration, the instrumental drift correction, and the computation of precise RVs and bisector spans, which are presented in Table 3. The four FEROS spectra were combined in order to measure the atmospheric parameters using the `zaspe` package (Brahm et al. 2017b), obtaining $T_{\rm eff} = 5669 \pm 80$ K, $\log g = 4.21 \pm 0.12$, [Fe/H] $= 0.28 \pm 0.05$ dex, and $v\sin i = 6.45 \pm 0.30$ km/s for TOI-569.

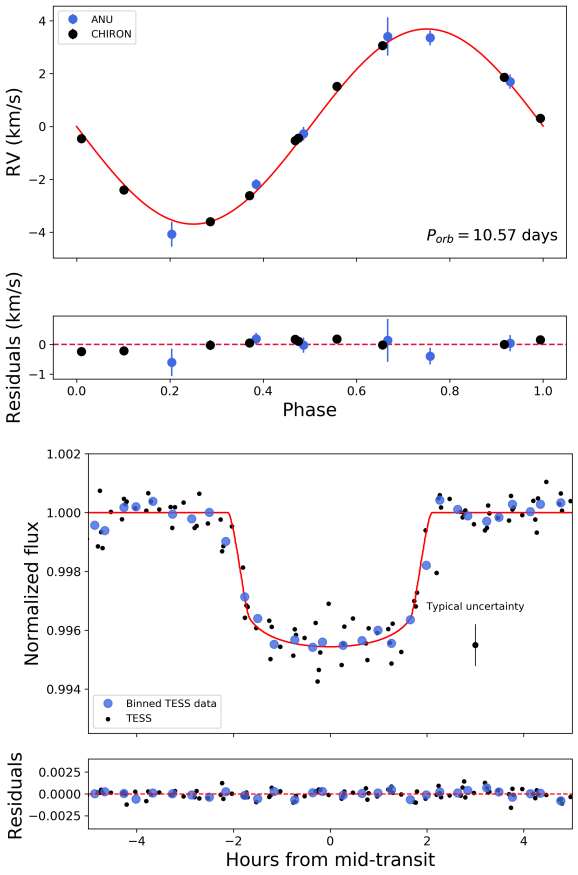

Figure 5. *Top*: Relative radial velocities of TOI-1406 with `EXOFASTv2` orbital solution plotted in red. *Bottom*: TESS light curve with `EXOFASTv2` transit model in red.

3. ANALYSIS

3.1. *Modeling with* `EXOFASTv2`

The masses and radii of the BDs are derived using `EXOFASTv2`. A full description of `EXOFASTv2` is given in Eastman et al. (2019). `EXOFASTv2` uses the Monte Carlo-Markov Chain (MCMC) method. For each MCMC fit, we use N=36 (N = 2×$n_{\rm parameters}$) walkers, or chains, and run for 50,000 steps, or links. To derive stellar parameters, `EXOFASTv2` utilizes the MIST isochrone models (Dotter 2016; Choi et al. 2016; Paxton et al. 2015) or the Yonsei-Yale isochrone models (YY; Spada et al. 2013). We use the MIST models for the analysis of TOI-1406 and the YY models for TOI-569. The YY models include a metallicity range of up to [Fe/H] = +0.78 dex while the MIST models currently implemented in `EXOFASTv2` extend [Fe/H] to only +0.5 dex. Based on our spectroscopic measurements of the metallicity for

TOI-569 (roughly +0.4), we choose to report the results for TOI-569 from the YY models in order to avoid approaching the upper limit on metallicity in the MIST models during the MCMC analysis. We see a difference of 0.1 dex between the metallicity found by the MIST models ($[\mathrm{Fe/H}]_{\mathrm{MIST}} = 0.30^{+0.14}_{-0.21}$ dex) to that found by the YY models ($[\mathrm{Fe/H}]_{\mathrm{YY}} = 0.40^{+0.07}_{-0.08}$ dex). The parameters for which we set priors and the types of priors we set for each (i.e. uniform $\mathcal{U}[a, b]$ or Gaussian $\mathcal{G}[a, b]$) are shown in Tables 7 and 8. We rely on our spectroscopic measurements and parallax measurements from *Gaia* to define our Gaussian priors, which penalize the fit for straying beyond the width, b, away from the mean, a of the parameter. We use an upper limit for the A_V extinction. See Table 3 of Eastman et al. (2019) for a detailed description of priors in `EXOFASTv2`. The spectral energy distribution for each star is also taken into account with `EXOFASTv2` and this is discussed in more depth in Section 3.3.

We also see bimodality in the posterior distribution for the age (and correlated parameters) of TOI-569, so we present the two most probable solutions resulting from the bimodal posterior distributions with the absolute most probable solution taken as the final reported value (Table 8). The most relevant bimodal posterior distributions are shown in Figure 6. The probability of the solution we report here is 0.73, with the less likely solution having a probability of 0.27.

3.2. *Analysis with* `pyaneti`

As an independent check on our `EXOFASTv2` analysis, we also carried out an analysis with the `pyaneti`[2] (Barragán et al. 2019) software. Using a Bayesian approach combined with MCMC sampling, we performed a joint analysis of the RV measurements and the TESS light curves and modelled posterior distributions of the fitted parameters. The RV data were fitted with Keplerian orbits, and for each different instrumental set-up, an offset term for each systemic velocity was included. The photometric data are modeled with the quadratic limb-darkening model of Mandel & Agol (2002).

We use uniform priors and fit for the BD-to-star radius ratio, the orbital period, the mid-transit time, the scaled orbital distance, the eccentricity, the argument of periastron, the impact parameter (b), and the Doppler semi-amplitude variation (K). The allowed ranges for the fit parameters for `pyaneti` are shown in Table 4.

We used 500 independent chains, and checked for convergence after every 5,000 iterations. After convergence, a posterior distribution of 250,000 independent points

[2] https://github.com/oscaribv/pyaneti

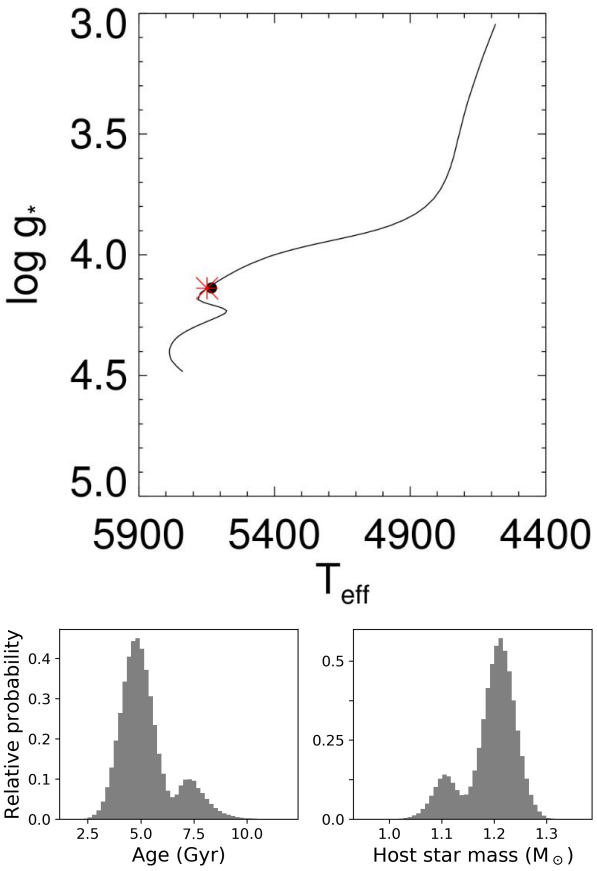

Figure 6. *Top*: Yonsei-Yale isochrone from `EXOFASTv2`. The black line is the best-fitting evolutionary mass track from the YY models. The black circle is the YY model value for $\log g$ and T_{eff}. The red asterisk corresponds to the model value of the age for TOI-569 (see Eastman et al. (2019), Table 3 for full details). The bimodality of the `EXOFASTv2` solution arises because TOI-569 falls near the main sequence turnoff point (the sharp bends in the black line). *Bottom*: Age and stellar mass posterior distributions from `EXOFASTv2` (YY) for TOI-569. We show these to provide a sense of the relative probabilities between the peaks of the bimodal distributions, which is roughly 3-to-1 in favor of a more massive, younger system. We see no bimodality for the posterior distributions of TOI-1406 in `EXOFASTv2`.

for every parameter was computed from the last 5,000 iterations. The eccentricity was found to be consistent with zero for both BDs.We find a mass and radius of TOI-569b and TOI-1406b to be consistent within 1-σ of the values from the `EXOFASTv2` models.

3.3. *Stellar parameters from broadband photometry*

As an independent check on the derived stellar parameters, we performed an analysis of the broadband spectral energy distribution (SED) together with the *Gaia* DR2 parallax in order to determine an empirical measurement of the stellar radius, following the procedures

Table 4. Allowed ranges for fit parameters from `pyaneti`.

Parameter	TOI-569	TOI-1406
$R_{\rm BD}/R_\star$	[0, 0.1]	[0, 0.1]
$P_{\rm orb}$ (days)	[6.5541, 6.5580]	[10.5721, 10.5762]
$T_0 - 2458400$ (BJD$_{\rm TDB}$)	[96.858, 96.878]	[14.5061, 14.7061]
$a/R_\star$	[1.1, 12]	[1.1, 19]
$e\cos\omega$	[-1, 1]	[-1, 1]
$e\sin\omega$	[-1, 1]	[-1, 1]
Impact parameter b	[0, 1]	[0, 1]
Semi-amplitude K (km/s)	[0, 15]	[0, 15]

described in Stassun & Torres (2016); Stassun et al. (2017, 2018a). We pulled the B_TV_T magnitudes from *Tycho-2*, the Strömgren ubvy magnitudes from Paunzen (2015), the BVgri magnitudes from APASS, the JHK_S magnitudes from *2MASS*, the W1–W4 magnitudes from *WISE*, and the G magnitude from *Gaia*. Together, the available photometry spans the full stellar SED over the wavelength range 0.35–22 μm (see Figure 7). We performed a fit using Kurucz stellar atmosphere models, with the priors on $T_{\rm eff}$, $\log g$, and [Fe/H] from the spectroscopically determined values. The remaining free parameter is the extinction (A_V), which we restricted to the maximum line-of-sight value from the dust maps of Schlegel et al. (1998).

Doing this yields stellar parameters that are consistent with those derived with `EXOFASTv2` with the mass and radius for TOI-569 being $M_\star = 1.26 \pm 0.08\,{\rm M}_\odot$ and $R_\star = 1.469 \pm 0.052\,{\rm R}_\odot$, and the mass and radius for TOI-1406 being $M_\star = 1.28 \pm 0.08\,{\rm M}_\odot$ and $R_\star = 1.308 \pm 0.048\,{\rm R}_\odot$. The stellar mass is determined from mass-radius relations from Torres et al. (2010). The resulting SED fits are shown in Figure 7.

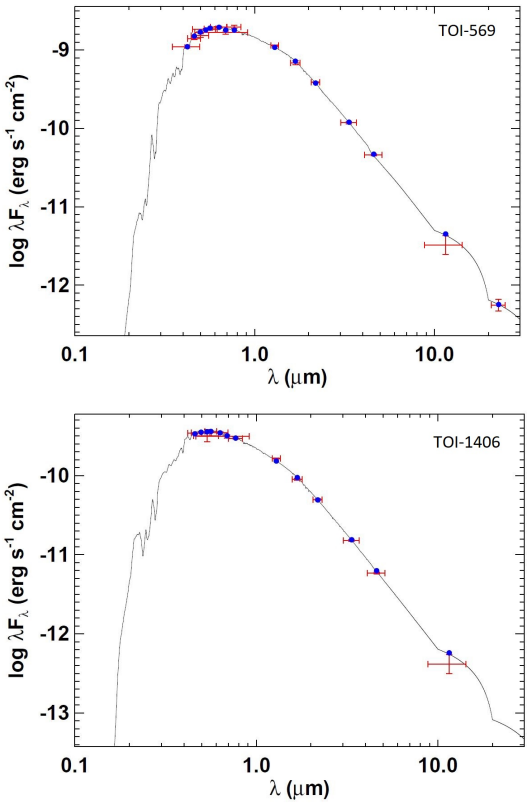

Figure 7. Spectral energy distributions for TOI-569 and TOI-1406. Red symbols represent the observed photometric measurements, where the horizontal bars represent the effective width of the bandpass. Blue symbols are the model fluxes from the best-fit Kurucz atmosphere model (black).

3.4. *Circularization and synchronization timescales*

In previous works (Persson et al. 2019; Subjak et al. 2019), we have calculated the timescale for the orbital period of an intermediate-mass BDs to synchronize with the rotation of their host star and to have their orbit circularized. In the case of EPIC 212036875b, a short-period BD with mass $M_b = 51 \pm 2\,{\rm M_J}$, Persson et al. (2019) found that the BD still has some orbital eccentricity ($e = 0.132$) and its current orbital configuration is a result of a relatively quick inward migration, favoring a formation scenario that the BD did not form at or near its current orbital configuration (i.e., not in-situ). In the case of TOI-503b, Subjak et al. (2019) find a relatively young (∼180 Myr) A-type host star with a BD ($M_b = 53.7\,{\rm M_J}$) in a circular orbit. This system has been more complex to describe with established tidal interaction models (e.g. Jackson et al. 2008) given that these models are not tailored to A-type stars with radiative envelopes and BD companions as massive as TOI-503b. Given this, Subjak et al. (2019) do not conclusively determine a formation scenario for TOI-503b (in-situ versus not) and instead offer some discussion of the tidal quality factors, Q, that may be most appropriate for this system. Here, we will examine the circularization timescales for TOI-569 and TOI-1406 in a similar way.

Following the formalism from Jackson et al. (2008), the equations for orbital circularization timescale for a close-in companion are:

$$\frac{1}{\tau_{\rm circ,\star}} = \frac{171}{16}\sqrt{\frac{G}{M_\star}}\frac{R_\star^5 M_{\rm BD}}{Q_\star}a^{-\frac{13}{2}} \quad (1)$$

$$\frac{1}{\tau_{\rm circ,BD}} = \frac{63}{4}\frac{\sqrt{GM_\star^3}R_{\rm BD}^5}{Q_{\rm BD}M_{\rm BD}}a^{-\frac{13}{2}} \quad (2)$$

$$\frac{1}{\tau_{\rm e}} = \frac{1}{\tau_{\rm circ,\star}} + \frac{1}{\tau_{\rm circ,BD}} \quad (3)$$

where $\tau_{\rm e}$ is the circularization timescale, a is the semi-major axis, $M_\star$ is the stellar mass, $R_\star$ is the stellar ra-

Table 5. Circularization timescales for different values of $Q_\star$ and $Q_{\rm BD}$ with stellar rotational period and BD orbital period. These rotation periods are calculated using $v \sin i$ and $R_\star$. Note for TOI-1406, the shortest $\tau_{\rm e}$ for reasonable choices of $Q_\star = 10^7$ and $Q_{\rm BD} = 10^{4.5}$ is $\tau_{\rm e} = 91.5^{+18.4}_{-17.0}$ Gyr. These show 1-σ uncertainties.

Object name & Age	$Q_\star$	$Q_{\rm BD}$	$\tau_{\rm e}$ (Gyr)
TOI-569	10^8	10^6	$78.6^{+7.7}_{-11.7}$
$4.79^{+0.73}_{-0.73}$ Gyr	10^8	$10^{4.5}$	$47.0^{+5.2}_{-7.4}$
	10^7	10^6	$8.0^{+0.8}_{-1.2}$
	10^7	$10^{4.5}$	$7.5^{+0.7}_{-1.1}$
	$P_{\rm rot}$ (days)	$P_{\rm orb}$ (days)	$v \sin i$ (km/s)
TOI-569	11.3	6.6	6.7 ± 0.1
TOI-1406	4.5	10.6	15.0 ± 1.0

dius, $M_{\rm BD}$ is the BD mass, $R_{\rm BD}$ is the BD radius, $Q_\star$ is the tidal quality factor for the star, and $Q_{\rm BD}$ is the tidal quality factor for the BD. The individual contributions of the effects of tides raised on the star and the BD are accounted for in Equations 1 & 2, respectively, and summed together in Equation 3. Equation 3 is a prediction on how long it takes for the orbital eccentricity of an object to decrease by an exponential factor (the relationship $\tau_{\rm e} \propto dt \propto -de/e$). Use of this equation comes with a number of assumptions that we reiterate here from Jackson et al. (2008): 1) the BD is in a short orbital period (10 days or less), 2) the orbital eccentricity e is small (though for companions in the planetary mass range, higher-order terms may be important to account for higher e in the past), 3) the BD's orbital period $P_{\rm orb}$ is smaller than the host star's rotation period $P_{\rm rot}$. Admittedly, Equation 3 and these assumptions cater to hot Jupiters and not much more massive BDs, which is important to highlight as $P_{\rm rot}$ of the host star is influenced by the presence of a massive companion. We also note that Equation 3 produces longer estimates for the circularization timescale compared to solutions worked out by Zahn (1977) and others, which predict tidal evolution to occur on shorter timescales.

We also highlight that the circularization timescale and the synchronization timescale, τ_Ω, change over time as the host star and especially the BD change in radius. The equation for τ_Ω from Goldreich & Soter (1966) is:

$$\frac{1}{\tau_\Omega} = \frac{9}{4} \frac{G R_\star^3 M_{\rm BD}^2}{\alpha_\star M_\star Q_\star \Omega a^6} \quad (4)$$

where $\Omega_\star$ is the angular velocity of the star and $\alpha_\star$ is the stellar moment of inertia.

With these considerations in mind, we calculate $\tau_{\rm e}$ for TOI-569b and TOI-1406b for a range of $Q_\star$ and Q_{BD}

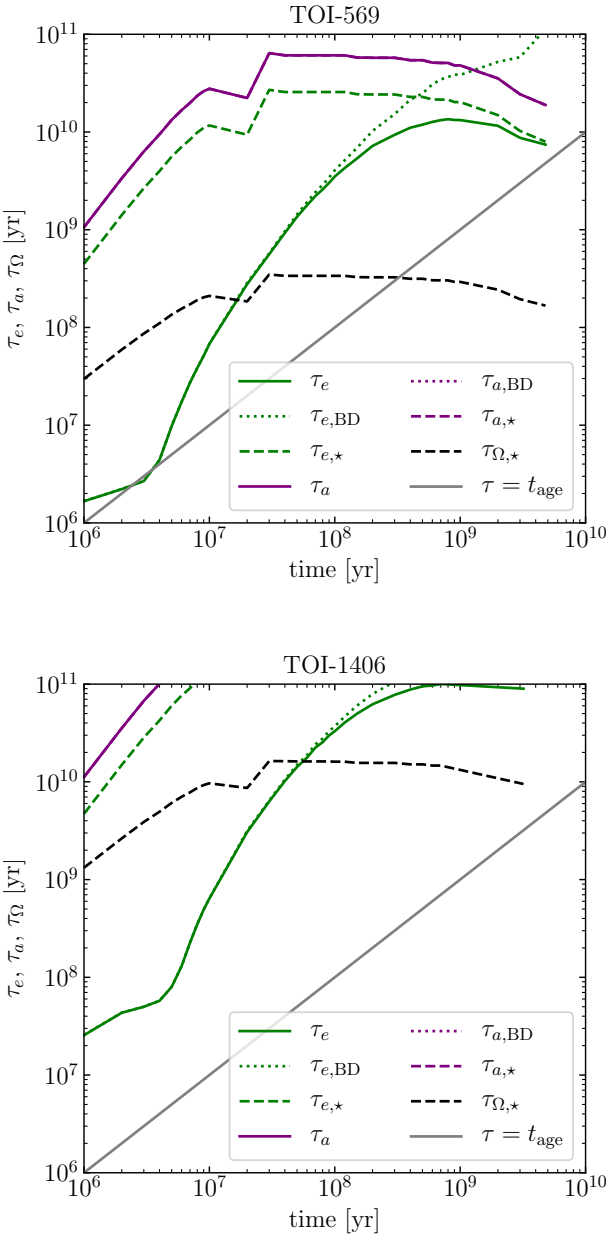

Figure 8. Circularization and synchronization timescales for TOI-569 and TOI-1406 as a function of the age of the system. Here we took tidal quality factors $Q_\star = 10^7$ and $Q_{\rm BD} = 10^{4.5}$. When the curves for τ_e, τ_a, or τ_Ω are above the solid line, then the respective timescale is longer than that current age of the system.

for each system in Table 5. The rotation period of each star is estimated using the projected rotation rate $v \sin i$ and the radius of the star from `EXOFASTv2`. The choice to adopt a $Q_{\rm BD}$ as low as $10^{4.5}$ comes from Beatty et al. (2018), who directly constrain $Q_{\rm BD}$ for CWW 89Ab, a $M_{\rm BD} = 39\,{\rm M_J}$ BD. For the bimodal posterior distribu-

tions of TOI-569, we only use the most probable $M_\star$, $R_\star$, $M_{\rm BD}$, $R_{\rm BD}$, and a (Table 8). Each parameter ($M_\star$, $R_\star$, $M_{\rm BD}$, $R_{\rm BD}$, and a) is a randomly sampled posterior distribution from `EXOFASTv2` and so the $\tau_{\rm e}$ distribution is as well. From the $\tau_{\rm e}$ distribution for our selected combinations of $Q_\star$ and $Q_{\rm BD}$, we calculate the median and 1-σ uncertainties as the 16$^{\rm th}$ and 84$^{\rm th}$ percentiles of the distribution. For TOI-569, we find a range of $\tau_{\rm e} = 7.5$ Gyr to $\tau_{\rm e} = 78.6$ Gyr. For TOI-1406, we see $\tau_{\rm e} > 91$ Gyr for the lowest reasonable choices of tidal quality factors, however, since $P_{\rm orb} > P_{\rm rot}$ in this system, these timescales are generally invalid. We also note that Jackson et al. (2008) provide equations for the orbital decay timescale τ_a and for both TOI-569 and TOI-1406, the decay timescale is at least an order of magnitude longer than the age of either system.

We see from Table 5 and Figure 8 that all reasonable choices of $Q_\star$ and $Q_{\rm BD}$ for TOI-1406 yield $\tau_{\rm e}$ and τ_Ω values much longer that the system's likely age ($3.20^{+2.20}_{-1.60}$ Gyr), but TOI-1406 does not meet the assumptions accounted for with Equation 3. Namely, the orbital period of TOI-1406b is *not* much shorter than the star's rotation period. In fact, $P_{\rm orb}$ of the BD is more than twice as long as $P_{\rm rot}$ for the star.

The narrative is different for TOI-569. In this system, $P_{\rm orb} < P_{\rm rot}$ and we find for certain permutations of $Q_\star$ and $Q_{\rm BD}$ that $\tau_{\rm e}$ is comparable to the age of TOI-569 (4.79 ± 0.73 Gyr). Additionally, this system is predicted to synchronize within 1 Gyr, yet we see from the TESS light curve (Figure 2) and $P_{\rm rot}$ derived from $v \sin i$ and $R_\star$ that the system is not synchronized. In order to explain why the stellar rotation and BD orbital period are *not* synchronized ($P_{\rm orb} \neq P_{\rm rot}$), a value of $Q_\star = 10^8$ is more appropriate for TOI-569. This is because higher values of Q indicate that the star or BD is more resistant to circularization or synchronization, which makes the timescales for these processes longer. A high value for $Q_\star$ is consistent with recent statistical estimates by Collier Cameron & Jardine (2018) and theoretical calculations by Penev & Sasselov (2011).

4. DISCUSSION

Including the new BDs in this work, the total number of known BDs that transit a star is 23 (Table 6). With the discovery of TOI-569b and TOI-1406b, the total number of new transiting BDs discovered or observed by the TESS mission is now 4 (Subjak et al. 2019; Jackman et al. 2019, this work). We expect at least as many more to be discovered as TESS continues its observations over the remainder of its primary mission. At present, we do not have enough transiting BDs to perform a statistical study of the population and draw conclusions about the fundamental origins of BDs and how the mass of a BD precisely reflects its formation and evolution.

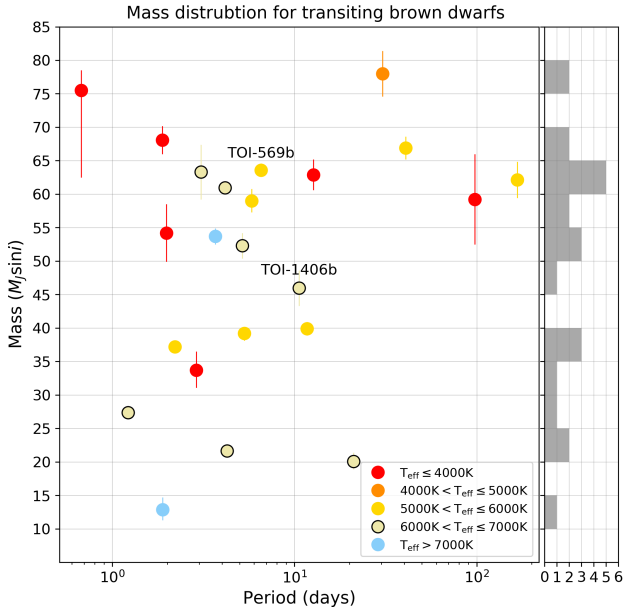

Figure 9. Mass-period distribution of transiting BDs. The colors indicate the effective temperature of the host star of each BD.

The mass distribution for the current population of BDs is shown in Figure 9 with the effective temperature of the host star indicated by the colors of the points. From all published studies of transiting BDs to date, there is no preference for a particular type of host star to BDs. This could be compared to the distribution of primary stars in short-period binary systems and to hot Jupiter host stars in future works once the total number of transiting BDs increases. Interestingly, we see that 6 transiting BDs (roughly 20% of the transiting BD population, see Table 6) are hosted by an M dwarf star. This is in contrast to hot Jupiters where only a few percent of the hot Jupiter population are found transiting M dwarf stars (e.g. Kepler-45b Johnson et al. (2012), HATS-6b Hartman et al. (2015), WASP-80b Triaud et al. (2015), NGTS-1b Bayliss et al. (2018)). It may be the case as TESS completes its primary mission that we continue to discover more BDs around M dwarfs. If so, we will be challenged to explain why this is the case for BDs and less so for giant planets.

4.1. *TOI-569b and TOI-1406b in the mass-radius diagram*

The mass-radius diagram for transiting BDs is shown in Figure 10. All of the BDs on this diagram are necessarily transiting because it is through the transit method

that we can measured the radius. However, even though a transit provides some measure of the radius, the measurement is not always very precise. Exactly how precise can be quantified with the aid of substellar evolutionary models (Baraffe et al. 2003, COND03). For example, we see from Figure 10 that an uncertainty of 0.3 R_J (∼30%) for any BD mass translates to an uncertainty of hundreds to thousands of Myr. These large (10-30%) uncertainties in the radii typically arise from grazing transits of the BDs, as is the case with CoRoT-33b (Csizmadia et al. 2015), NLTT 41135b (Irwin et al. 2010), and TOI-503b (Subjak et al. 2019). So, what may seem to be a reasonably precise radius uncertainty of 10% actually turns out to be a rather large uncertainty in the age.

We are fortunate that the transits of TOI-569b and TOI-1406b are not grazing, which means we have a nicely constrained measurement (< 5% uncertainty) of the radius of each BD. This means that these two new transiting BDs have precisely predicted ages from substellar evolutionary models. The COND03 models consider the effects of irradiation on the BD's radius over time, while another set of models by Saumon & Marley (2008) (SM08) does not and instead focuses on the effects of metallicity.

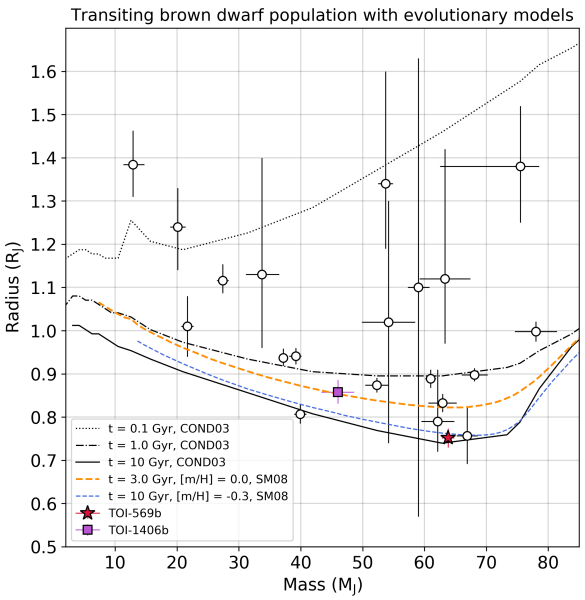

Figure 10. Mass-radius diagram of transiting BDs featuring the Baraffe et al. (2003) (COND03) and Saumon & Marley (2008) (SM08) models. TOI-569b and TOI-1406b are shown as a red star and a purple square, respectively. Both models overestimate the age of TOI-569b yet seem to approximately estimate the age of TOI-1406b.

We see that both sets of models seem to overestimate the age of TOI-569b to be ∼10 Gyr compared to the age of the host star modelled from MIST (4.79 ± 0.73 Gyr). For TOI-1406, we find that both the COND03 and SM08 models roughly predict the age of the system ($3.20^{+2.20}_{-1.60}$ Gyr). This is difficult to reconcile since the COND03 and SM08 models overestimate the age of the TOI-569b while these same models reasonably predict the age of TOI-1406b. It may be that the age of TOI-1406b is only coincidentally predicted and that more generally these models overestimate a BD's age. Evidence for this may be seen in how both models overestimate the ages of CWW 89Ab (Beatty et al. 2018) and AD 3116b Gillen et al. (2017), which are two BDs with directly measured ages via their association with stellar clusters/streams. Another way to convey this is to say that the COND03 models may *underestimate* the rate at which irradiated, short-period transiting BDs contract over long timescales.

4.2. *Possible formation pathways for TOI-569b and TOI-1406b*

Though the COND03 and SM08 models may not accurately estimate the ages of these BDs, we do have reasonable estimates of the ages of the host stars. So, we may compare the Jackson et al. (2008) models for circularization and synchronization timescales to these ages. We do this in an effort to find evidence in favor of a formation scenario for short-period BDs that is either more similar to that of giant planets or instead more similar to the formation of the smallest, least massive stars. The different types of formation pathways can be broadly reduced into three methods: 1) cloud fragmentation, 2) gravitational disk instability, 3) core accretion in a protoplanetary disk. Considering now the short-period BDs in this study, each of these possible BD pathways may happen at different distances from a host star and somehow result in a close-in BD. Given this, we may break down these pathways further into three scenarios:

Scenario 1: formation *in-situ* at or very close to the BD's current orbit

Scenario 2: formation in a disk at a wide separation from the host star and a slow or "dynamically quiet" migration inward

Scenario 3: formation in a disk at a high eccentricity with tidal damping aiding in migration inward to a circular orbit

Now, we may examine each scenario in the context of the three aforementioned formation pathways (cloud fragmentation, gravitational instability, core accretion). Note that we have ruled out Scenario 3 for all formation pathways in Section 3.4 (see Table 5 and Figure 8).

4.2.1. *Cloud or core fragmentation in the disk*

Scenario 1 is not possible for TOI-569b and TOI-1406b because fragmentation has been shown to occur on scales of tens to thousands of AU (Delgado-Donate et al. 2004; Offner et al. 2010; Bate 2019), so in-situ cloud fragmentation cannot happen at the orbital separations of these BDs. Scenario 2 may be possible although the migration through the disk will take place after formation through the dissipative interactions with gases in the disk. Scenario 2 also faces resistance in that disk evolutionary models do not produce BDs at sub-AU scales very well.

4.2.2. *Gravitational disk instability*

Scenario 1 for in-situ formation cannot happen in the case of either BD due to high disk temperatures and a Toomre $Q > 1$ at scales of a few AU or less (Kratter & Lodato 2016). With the ideal conditions, Scenario 2 is possible. That is, single or multiple fragments may form at wide separations (30-100 AU) from the host star and migrate inward. Single fragments may even migrate quickly if they avoid gap openings in the disk as the travel inward (Malik et al. 2015; Stamatellos & Inutsuka 2018). This sort of migration is enhanced when multiple fragments form (Forgan et al. 2018). Whether or not these fragments can migrate inward while maintaining a nearly circular orbit and build to a single 40-65 M_J object is unclear.

4.2.3. *Core accretion in the disk*

Scenario 1 is not possible given the large masses of TOI-569b and TOI-1406b. Hot Jupiters may be able to form in-situ with a sufficiently massive enough core ($15M_\oplus$, Coleman et al. 2017), but it is not clear that this scales to 40-50 M_J. Scenario 2 is not possible for similar reasons; the mass budget for gas in the disk may not be high enough to grow a core to tens of Jupiter masses. Though with TOI-569, the high metallicity helps in massive core growth (Mordasini et al. 2012), this does not appear to explain the resulting 63 M_J BD.

Though a clear explanation has yet to present itself, it seems that TOI-569b and TOI-1406b may have formed in nearly circular orbits and migrated inwards in such a way to maintain their zero eccentricity over a few billion years.

Ultimately, we find TOI-569b and TOI-1406b to be special in that they contribute new measurements to the still sparsely populated mass-radius diagram for transiting BDs. These systems also offer themselves as new data to examine circularization and synchronization models. As we continue to characterize new short-period, intermediate mass BDs, we are learning that no single formation scenario seems to adequately describe these type of BDs. Perhaps then, it is the systems like TOI-569 and TOI-1406 that may be the most informative in our endeavors to understand BD formation.

5. ACKNOWLEDGEMENTS

TWC acknowledges the efforts of the members of the TESS Followup Program and the Science Processing Operations Center in making the TESS data readily accessible for the analysis in this work.

Funding for this work is provided by the National Science Foundation Graduate Research Fellowship Program Fellowship (GRFP). This work makes use of observations from the LCO network.

AJM acknowledges support from the Knut & Alice Wallenberg Foundation (project grant 2014.0017) and the Walter Gyllenberg Foundation of the Royal Physiographical Society in Lund.

CMP and MF gratefully acknowledge the support of the Swedish National Space Agency (DNR 163/16).

REFERENCES

Anderson, D. R., Collier Cameron, A., Hellier, C., et al. 2011, ApJL, 726, L19

Baraffe, I., Chabrier, G., Barman, T. S., Allard, F., & Hauschildt, P. H. 2003, A&A, 402, 701

Barragán, O., Gandolfi, D., & Antoniciello, G. 2019, MNRAS, 482, 1017

Bate, M. R. 2019, MNRAS, 484, 2341

Bayliss, D., Hojjatpanah, S., Santerne, A., et al. 2017, AJ, 153, 15

Bayliss, D., Gillen, E., Eigmüller, P., et al. 2018, MNRAS, 475, 4467

Beatty, T. G., Morley, C. V., Curtis, J. L., et al. 2018, AJ, 156, 168

Bonomo, A. S., Sozzetti, A., Santerne, A., et al. 2015, A&A, 575, A85

Bouchy, F., Deleuil, M., Guillot, T., et al. 2011, A&A, 525, A68

Brahm, R., Jordán, A., & Espinoza, N. 2017a, PASP, 129, 034002

Brahm, R., Jordán, A., Hartman, J., & Bakos, G. 2017b, MNRAS, 467, 971

Brown, T. M., Baliber, N., Bianco, F. B., et al. 2013, Publications of the Astronomical Society of the Pacific, 125, 1031

Carmichael, T., Latham, D., & Vanderburg, A. 2019, arXiv e-prints, arXiv:1903.03118

Castelli, F., & Kurucz, R. L. 2004, ArXiv Astrophysics e-prints, astro-ph/0405087
Choi, J., Dotter, A., Conroy, C., et al. 2016, ApJ, 823, 102
Coleman, G. A. L., Papaloizou, J. C. B., & Nelson, R. P. 2017, MNRAS, 470, 3206
Collier Cameron, A., & Jardine, M. 2018, MNRAS, 476, 2542
Collins, K. A., Kielkopf, J. F., Stassun, K. G., & Hessman, F. V. 2017, AJ, 153, 77
Csizmadia, S., & CoRot Team. 2016, III.6 Exploration of the brown dwarf regime around solar-like stars by CoRoT, 143
Csizmadia, S., Hatzes, A., Gandolfi, D., et al. 2015, A&A, 584, A13
Cutri, R. M., & et al. 2013, VizieR Online Data Catalog, II/328
Cutri, R. M., Skrutskie, M. F., van Dyk, S., et al. 2003, VizieR Online Data Catalog, II/246
David, T. J., Hillenbrand, L. A., Gillen, E., et al. 2019, ApJ, 872, 161
Deleuil, M., Deeg, H. J., Alonso, R., et al. 2008, A&A, 491, 889
Delgado-Donate, E. J., Clarke, C. J., Bate, M. R., & Hodgkin, S. T. 2004, MNRAS, 351, 617
Díaz, R. F., Damiani, C., Deleuil, M., et al. 2013, A&A, 551, L9
Díaz, R. F., Montagnier, G., Leconte, J., et al. 2014, A&A, 572, A109
Donati, J.-F., Semel, M., Carter, B. D., Rees, D. E., & Collier Cameron, A. 1997, MNRAS, 291, 658
Dotter, A. 2016, ApJS, 222, 8
Eastman, J. D., Rodriguez, J. E., Agol, E., et al. 2019, arXiv e-prints, arXiv:1907.09480
Forgan, D. H., Hall, C., Meru, F., & Rice, W. K. M. 2018, MNRAS, 474, 5036
Gaia Collaboration, Brown, A. G. A., Vallenari, A., et al. 2018, A&A, 616, A1
Gillen, E., Hillenbrand, L. A., David, T. J., et al. 2017, ApJ, 849, 11
Goldreich, P., & Soter, S. 1966, Icarus, 5, 375
Gray, D. F. 2005, The Observation and Analysis of Stellar Photospheres
Hartman, J. D., Bayliss, D., Brahm, R., et al. 2015, AJ, 149, 166
Hodžić, V., Triaud, A. H. M. J., Anderson, D. R., et al. 2018, MNRAS, 481, 5091
Høg, E., Fabricius, C., Makarov, V. V., et al. 2000, A&A, 355, L27
Irwin, J., Buchhave, L., Berta, Z. K., et al. 2010, ApJ, 718, 1353
Irwin, J. M., Charbonneau, D., Esquerdo, G. A., et al. 2018, AJ, 156, 140
Jackman, J. A. G., Wheatley, P. J., Bayliss, D., et al. 2019, arXiv e-prints, arXiv:1906.08219
Jackson, B., Greenberg, R., & Barnes, R. 2008, ApJ, 678, 1396
Jensen, E. 2013, Tapir: A web interface for transit/eclipse observability, Astrophysics Source Code Library, , , ascl:1306.007
Johnson, J. A., Apps, K., Gazak, J. Z., et al. 2011, ApJ, 730, 79
Johnson, J. A., Gazak, J. Z., Apps, K., et al. 2012, AJ, 143, 111
Kaufer, A., & Pasquini, L. 1998, in Proc. SPIE, Vol. 3355, Optical Astronomical Instrumentation, ed. S. D'Odorico, 844–854
Kratter, K., & Lodato, G. 2016, ARA&A, 54, 271
Lightkurve Collaboration, Cardoso, J. V. d. M., Hedges, C., et al. 2018, Lightkurve: Kepler and TESS time series analysis in Python, Astrophysics Source Code Library, , , ascl:1812.013
Lindegren, L., Hernández, J., Bombrun, A., et al. 2018, A&A, 616, A2
Ma, B., & Ge, J. 2014, MNRAS, 439, 2781
Malik, M., Meru, F., Mayer, L., & Meyer, M. 2015, ApJ, 802, 56
Mandel, K., & Agol, E. 2002, ApJL, 580, L171
Marcy, G. W., & Butler, R. P. 2000, PASP, 112, 137
Mordasini, C., Alibert, Y., Klahr, H., & Henning, T. 2012, A&A, 547, A111
Moutou, C., Bonomo, A. S., Bruno, G., et al. 2013, A&A, 558, L6
Nowak, G., Palle, E., Gandolfi, D., et al. 2017, AJ, 153, 131
Offner, S. S. R., Kratter, K. M., Matzner, C. D., Krumholz, M. R., & Klein, R. I. 2010, ApJ, 725, 1485
Paunzen, E. 2015, A&A, 580, A23
Paxton, B., Marchant, P., Schwab, J., et al. 2015, ApJS, 220, 15
Penev, K., & Sasselov, D. 2011, ApJ, 731, 67
Pepe, F., Mayor, M., Rupprecht, G., et al. 2002, The Messenger, 110, 9
Persson, C. M., Csizmadia, S., Mustill, A. e. J., et al. 2019, A&A, 628, A64
Queloz, D., Mayor, M., Udry, S., et al. 2001, The Messenger, 105, 1
Saumon, D., & Marley, M. S. 2008, ApJ, 689, 1327
Schlegel, D. J., Finkbeiner, D. P., & Davis, M. 1998, ApJ, 500, 525
Siverd, R. J., Beatty, T. G., Pepper, J., et al. 2012, ApJ, 761, 123

Smith, J. C., Stumpe, M. C., Van Cleve, J. E., et al. 2012, PASP, 124, 1000

Spada, F., Demarque, P., Kim, Y.-C., & Sills, A. 2013, ApJ, 776, 87

Stamatellos, D., & Inutsuka, S.-i. 2018, MNRAS, 477, 3110

Stassun, K. G., Collins, K. A., & Gaudi, B. S. 2017, AJ, 153, 136

Stassun, K. G., Corsaro, E., Pepper, J. A., & Gaudi, B. S. 2018a, AJ, 155, 22

Stassun, K. G., Mathieu, R. D., & Valenti, J. A. 2006, Nature, 440, 311

Stassun, K. G., & Torres, G. 2016, arXiv e-prints, arXiv:1609.05390

Stassun, K. G., Oelkers, R. J., Pepper, J., et al. 2018b, AJ, 156, 102

Stumpe, M. C., Smith, J. C., Catanzarite, J. H., et al. 2014, PASP, 126, 100

Subjak, J., Sharma, R., Carmichael, T. W., et al. 2019, arXiv e-prints, arXiv:1909.07984

Tokovinin, A. 2018, PASP, 130, 035002

Torres, G., Andersen, J., & Giménez, A. 2010, A&A Rv, 18, 67

Triaud, A. H. M. J., Gillon, M., Ehrenreich, D., et al. 2015, MNRAS, 450, 2279

Yee, S. W., Petigura, E. A., & von Braun, K. 2017, ApJ, 836, 77

Zahn, J.-P. 1977, A&A, 57, 383

Zhou, G., Bayliss, D., Hartman, J. D., et al. 2014, MNRAS, 437, 2831

Zhou, G., Bakos, G. Á., Bayliss, D., et al. 2019, AJ, 157, 31

Zhou, G., Bakos, G. Á., Bayliss, D., et al. 2019, The Astronomical Journal, 157, 31. https://doi.org/10.3847%2F1538-3881%2Faaf1bb

Ziegler, C., Tokovinin, A., Briceno, C., et al. 2019, arXiv e-prints, arXiv:1908.10871

Table 6. List of published transiting brown dwarfs as of September 2019.

Name	P (days)	M_{BD}/M_J	R_{BD}/R_J	e	$M_\star/M_\odot$	$R_\star/R_\odot$	T_{eff}(K)	[Fe/H]	Reference
TOI-569b	6.556	63.8 ± 1.0	0.75 ± 0.02	0 (adopted)	1.21 ± 0.03	1.48 ± 0.03	5705 ± 76	$+0.40 \pm 0.08$	this work
TOI-1406b	10.574	46.0 ± 2.7	0.86 ± 0.03	0 (adopted)	1.18 ± 0.09	1.35 ± 0.03	6290 ± 100	-0.08 ± 0.09	this work
HATS-70b	1.888	12.9 ± 1.8	1.38 ± 0.08	< 0.18	1.78 ± 0.12	1.88 ± 0.07	7930 ± 820	$+0.04 \pm 0.11$	1
KELT-1b	1.218	27.4 ± 0.9	1.12 ± 0.04	0.01 ± 0.01	1.34 ± 0.06	1.47 ± 0.05	6516 ± 49	$+0.05 \pm 0.08$	2
NLTT 41135b	2.889	33.7 ± 2.8	1.13 ± 0.27	< 0.02	0.19 ± 0.03	0.21 ± 0.02	3230 ± 130	-0.25 ± 0.25	3
LHS 6343c	12.713	62.9 ± 2.3	0.83 ± 0.02	0.056 ± 0.032	0.37 ± 0.01	0.38 ± 0.01	-	$+0.02 \pm 0.19$	4
LP 261-75b	1.882	68.1 ± 2.1	0.90 ± 0.02	< 0.007	0.30 ± 0.02	0.31 ± 0.01	3100 ± 50	-	5
WASP-30b	4.157	61.0 ± 0.9	0.89 ± 0.02	0 (adopted)	1.17 ± 0.03	1.30 ± 0.02	6201 ± 97	-0.08 ± 0.10	6
WASP-128b	2.209	37.2 ± 0.9	0.94 ± 0.02	< 0.007	1.16 ± 0.04	1.15 ± 0.02	5950 ± 50	$+0.01 \pm 0.12$	7
CoRoT-3b	4.257	21.7 ± 1.0	1.01 ± 0.07	0 (adopted)	1.37 ± 0.09	1.56 ± 0.09	6740 ± 140	-0.02 ± 0.06	8
CoRoT-15b	3.060	63.3 ± 4.1	1.12 ± 0.30	0 (adopted)	1.32 ± 0.12	1.46 ± 0.31	6350 ± 200	$+0.10 \pm 0.20$	9
CoRoT-33b	5.819	59.0 ± 1.8	1.10 ± 0.53	0.070 ± 0.002	0.86 ± 0.04	0.94 ± 0.14	5225 ± 80	$+0.44 \pm 0.10$	10
Kepler-39b	21.087	20.1 ± 1.3	1.24 ± 0.10	0.112 ± 0.057	1.29 ± 0.07	1.40 ± 0.10	6350 ± 100	$+0.10 \pm 0.14$	11
KOI-189b	30.360	78.0 ± 3.4	1.00 ± 0.02	0.275 ± 0.004	0.76 ± 0.05	0.73 ± 0.02	4952 ± 40	-0.07 ± 0.12	12
KOI-205b	11.720	39.9 ± 1.0	0.81 ± 0.02	< 0.031	0.92 ± 0.03	0.84 ± 0.02	5237 ± 60	$+0.14 \pm 0.12$	13
KOI-415b	166.788	62.1 ± 2.7	0.79 ± 0.12	0.689 ± 0.001	0.94 ± 0.06	1.15 ± 0.15	5810 ± 80	-0.24 ± 0.11	14
EPIC 201702477b	40.737	66.9 ± 1.7	0.76 ± 0.07	0.228 ± 0.003	0.87 ± 0.03	0.90 ± 0.06	5517 ± 70	-0.16 ± 0.05	15
EPIC 212036875b	5.170	52.3 ± 1.9	0.87 ± 0.02	0.132 ± 0.004	1.29 ± 0.07	1.50 ± 0.03	6238 ± 60	$+0.01 \pm 0.10$	18, 21
AD 3116b	1.983	54.2 ± 4.3	1.02 ± 0.28	0.146 ± 0.024	0.28 ± 0.02	0.29 ± 0.08	3200 ± 200	$+0.16 \pm 0.10$	17
CWW 89Ab	5.293	39.2 ± 1.1	0.94 ± 0.02	0.189 ± 0.002	1.10 ± 0.05	1.03 ± 0.02	5755 ± 49	$+0.20 \pm 0.09$	16, 18
RIK 72b	97.760	59.2 ± 6.8	3.10 ± 0.31	0.146 ± 0.012	0.44 ± 0.04	0.96 ± 0.10	3349 ± 142	-	19
TOI-503b	3.677	53.7 ± 1.2	$1.34^{+0.26}_{-0.15}$	0 (adopted)	1.80 ± 0.06	1.70 ± 0.05	7650 ± 160	$+0.61 \pm 0.07$	22
NGTS-7Ab	0.676	$75.5^{+3.0}_{-13.7}$	$1.38^{+0.13}_{-0.14}$	0 (adopted)	0.48 ± 0.13	0.61 ± 0.06	3359 ± 106	-	23
2M0535-05a[g]	9.779	56.7 ± 4.8	6.50 ± 0.33	0.323 ± 0.006	-	-	-	-	20
2M0535-05b[f]	9.779	35.6 ± 2.8	5.00 ± 0.25	0.323 ± 0.006	-	-	-	-	20

NOTE—References: 1 - Zhou et al. (2019), 2 - Siverd et al. (2012), 3 - Irwin et al. (2010), 4 - Johnson et al. (2011), 5 - Irwin et al. (2018), 6 - Anderson et al. (2011), 7 - Hodžić et al. (2018), 8 - Deleuil et al. (2008), 9 - Bouchy et al. (2011), 10 - Csizmadia et al. (2015), 11 - Bonomo et al. (2015), 12 - Díaz et al. (2014), 13 - Díaz et al. (2013), 14 - Moutou et al. (2013), 15 - Bayliss et al. (2017), 16 - Nowak et al. (2017), 17 - Gillen et al. (2017), 18 - Carmichael et al. (2019), 19 - David et al. (2019), 20 - Stassun et al. (2006), 21 - Persson et al. (2019), 22 - Subjak et al. (2019), 23 - Jackman et al. (2019)

Table 7. MIST median values and 68% confidence interval for TOI-1406, created using `EXOFASTv2` commit number 65aa674. Here, $\mathcal{U}$[a,b] is the uniform prior bounded between a and b, and $\mathcal{G}[a,b]$ is a Gaussian prior of mean a and width b.

Parameter	Units	Priors	Values
Stellar Parameters:			
M_*	Mass ($M_\odot$)	-	$1.18^{+0.08}_{-0.09}$
R_*	Radius ($R_\odot$)	-	$1.35^{+0.03}_{-0.03}$
L_*	Luminosity ($L_\odot$)	-	2.56 ± 0.15
ρ_*	Density (cgs)	-	$0.68^{+0.07}_{-0.07}$
$\log g$	Surface gravity (cgs)	-	$4.252^{+0.037}_{-0.041}$
$T_{\rm eff}$	Effective Temperature (K)	$\mathcal{G}[6282, 110]$	6290 ± 100
[Fe/H]	Metallicity (dex)	$\mathcal{G}[-0.09, 0.09]$	-0.08 ± 0.09
Age	Age (Gyr)	-	$3.20^{+2.20}_{-1.60}$
EEP	Equal Evolutionary Point	-	377^{+40}_{-36}
A_V	V-band extinction (mag)	$\mathcal{U}[0, 0.08804]$	$0.043^{+0.030}_{-0.029}$
σ_{SED}	SED photometry error scaling	-	$3.04^{+1.2}_{-0.73}$
ϖ	Parallax (mas)	$\mathcal{G}[2.3855, 0.0291]$	2.386 ± 0.029
d	Distance (pc)	-	$419.1^{+5.2}_{-5.0}$
Brown Dwarf Parameters:			
P	Period (days)	-	$10.57398^{+0.00060}_{-0.00059}$
M_P	Mass (M_J)	-	$46.0^{+2.6}_{-2.7}$
R_P	Radius (R_J)	-	0.86 ± 0.03
T_C	Time of conjunction (BJD_{TDB})	-	$2458414.6065^{+0.0018}_{-0.0019}$
T_0	Optimal conjunction Time (BJD_{TDB})	-	$2458435.7545^{+0.0012}_{-0.0011}$
a	Semi-major axis (AU)	-	$0.1010^{+0.0022}_{-0.0026}$
i	Inclination (Degrees)	-	$87.70^{+0.19}_{-0.20}$
e	Eccentricity	-	0 (adopted)
T_{eq}	Equilibrium temperature (K)	-	1108^{+18}_{-17}
K	RV semi-amplitude (m/s)	-	3720^{+120}_{-130}
$logK$	Log of RV semi-amplitude	-	$3.570^{+0.014}_{-0.015}$
R_P/R_*	Radius of planet in stellar radii	-	0.0654 ± 0.0011
a/R_*	Semi-major axis in stellar radii	-	$16.11^{+0.56}_{-0.58}$
δ	Transit depth (fraction)	-	0.00428 ± 0.00014
$Depth$	Flux decrement at mid transit	-	0.00428 ± 0.00014
τ	Ingress/egress transit duration (days)	-	$0.0180^{+0.0016}_{-0.0014}$
b	Transit Impact parameter	-	$0.648^{+0.033}_{-0.036}$
ρ_P	Density (cgs)	-	$90^{+11}_{-10.}$
$logg_P$	Surface gravity	-	$5.190^{+0.040}_{-0.042}$
$M_P \sin i$	Minimum mass (M_J)	-	$45.9^{+2.6}_{-2.7}$
M_P/M_*	Mass ratio	-	$0.0372^{+0.0016}_{-0.0015}$
Wavelength Parameters:		TESS band	
u_1	linear limb-darkening coeff	0.224 ± 0.050	
u_2	quadratic limb-darkening coeff	0.299 ± 0.050	
RV Parameters:		ANU	CHIRON
$\gamma_{\rm rel}$	Relative RV Offset (m/s)	-15490^{+200}_{-240}	-15461^{+70}_{-68}
σ_J	RV Jitter (m/s)	380^{+400}_{-260}	182^{+85}_{-56}
σ_J^2	RV Jitter Variance	$150000^{+460000}_{-130000}$	33000^{+38000}_{-17000}
Transit Parameters:		TESS	
σ^2	Added Variance	$-0.000000154^{+0.000000011}_{-0.000000010}$	
F_0	Baseline flux	0.999996 ± 0.000013	

Table 8. Yonsei-Yale median values and 68% confidence interval for TOI-569, created using `EXOFASTv2` commit number 65aa674. The most likely values (probability of 0.73) and the ones we report for this system are shown in boldface. Here, $\mathcal{U}$[a,b] is the uniform prior bounded between a and b, and $\mathcal{G}[a,b]$ is a Gaussian prior of mean a and width b.

Parameter	Units	Priors	**Most likely values**	Less likely values
Stellar Parameters:			**Prob. = 0.73**	Prob. = 0.27
M_*	Mass ($M_\odot$)	-	$\mathbf{1.21 \pm 0.03}$	$1.11^{+0.02}_{-0.03}$
R_*	Radius ($R_\odot$)	-	$\mathbf{1.48 \pm 0.03}$	1.48 ± 0.03
L_*	Luminosity ($L_\odot$)	-	$\mathbf{2.08^{+0.10}_{-0.09}}$	2.03 ± 0.09
ρ_*	Density (cgs)	-	$\mathbf{0.52 \pm 0.03}$	0.48 ± 0.03
$\log g$	Surface gravity (cgs)	-	$\mathbf{4.18 \pm 0.019}$	4.14 ± 0.02
$T_{\rm eff}$	Effective Temperature (K)	$\mathcal{G}[5605, 100]$	$\mathbf{5705^{+76}_{-68}}$	5651^{+60}_{-62}
[Fe/H]	Metallicity (dex)	$\mathcal{G}[0.41, 0.1]$	$\mathbf{0.40^{+0.07}_{-0.08}}$	0.33 ± 0.08
Age	Age (Gyr)	-	$\mathbf{4.79 \pm 0.73}$	$7.44^{+0.82}_{-0.58}$
A_V	V-band extinction (mag)	$\mathcal{U}[0, 1.1749]$	$\mathbf{0.067^{+0.083}_{-0.049}}$	$0.052^{+0.074}_{-0.038}$
σ_{SED}	SED photometry error scaling	-	$\mathbf{2.94^{+1.20}_{-0.71}}$	$3.08^{+1.40}_{-0.78}$
ϖ	Parallax (mas)	$\mathcal{G}[6.3723, 0.0306]$	$\mathbf{6.374 \pm 0.031}$	$6.374^{+0.031}_{-0.030}$
d	Distance (pc)	-	$\mathbf{156.88 \pm 0.75}$	156.83 ± 0.75
Brown Dwarf Parameters:				
P	Period (days)	-	$\mathbf{6.55604^{+0.00016}_{-0.00015}}$	$6.55603^{+0.00016}_{-0.00015}$
M_P	Mass (M_J)	-	$\mathbf{63.8 \pm 1.0}$	$60.1^{+0.8}_{-0.9}$
R_P	Radius (R_J)	-	$\mathbf{0.75 \pm 0.02}$	0.76 ± 0.02
T_C	Time of conjunction (BJD_{TDB})	-	$\mathbf{2458523.09192^{+0.00070}_{-0.00069}}$	$2458523.09199 \pm 0.00070$
T_0	Optimal conjunction Time (BJD_{TDB})	-	$\mathbf{2458529.64796^{+0.00070}_{-0.00068}}$	$2458529.64803^{+0.00070}_{-0.00069}$
a	Semi-major axis (AU)	-	$\mathbf{0.07428 \pm 0.00059}$	$0.07207^{+0.00047}_{-0.00069}$
i	Inclination (Degrees)	-	$\mathbf{85.37^{+0.13}_{-0.11}}$	$85.15^{+0.13}_{-0.12}$
e	Eccentricity	-	**0** (adopted)	0 (adopted)
T_{eq}	Equilibrium temperature (K)	-	$\mathbf{1227^{+13}_{-12}}$	1237^{+12}_{-13}
K	RV semi-amplitude (m/s)	-	$\mathbf{5884 \pm 17}$	5884^{+18}_{-17}
$logK$	Log of RV semi-amplitude	-	$\mathbf{3.7697 \pm 0.0013}$	3.7697 ± 0.0013
R_P/R_*	Radius of planet in stellar radii	-	$\mathbf{0.05217^{+0.00094}_{-0.00091}}$	$0.05258^{+0.0010}_{-0.00096}$
a/R_*	Semi-major axis in stellar radii	-	$\mathbf{10.81^{+0.22}_{-0.21}}$	$10.44^{+0.21}_{-0.20}$
δ	Transit depth (fraction)	-	$\mathbf{0.002721^{+0.00010}_{-0.000096}}$	$0.002765^{+0.00011}_{-0.000100}$
Depth	Flux decrement at mid transit	-	$\mathbf{0.002730^{+0.00010}_{-0.000096}}$	$0.002765^{+0.00011}_{-0.000100}$
τ	Ingress/egress transit duration (days)	-	$\mathbf{0.0214^{+0.0015}_{-0.0013}}$	$0.0230^{+0.0014}_{-0.0013}$
b	Transit Impact parameter	-	$\mathbf{0.8739^{+0.0082}_{-0.0084}}$	$0.8820^{+0.0068}_{-0.0075}$
ρ_P	Density (cgs)	-	$\mathbf{187^{+17}_{-16}}$	169^{+16}_{-15}
$logg_P$	Surface gravity	-	$\mathbf{5.444^{+0.029}_{-0.031}}$	$5.412^{+0.027}_{-0.026}$
$M_P \sin i$	Minimum mass (M_J)	-	$\mathbf{63.6 \pm 1.0}$	$59.9^{+0.8}_{-0.9}$
M_P/M_*	Mass ratio	-	$\mathbf{0.05043^{+0.00097}_{-0.00050}}$	$0.05195^{+0.00045}_{-0.00039}$
Wavelength Parameters:		I-band	TESS band	
u_1	linear limb-darkening coeff	0.292 ± 0.050	0.335 ± 0.049	
u_2	quadratic limb-darkening coeff	0.260 ± 0.050	0.269 ± 0.049	
RV Parameters:		CHIRON	CORALIE	FEROS
$\gamma_{\rm rel}$	Relative RV Offset (m/s)	71964^{+14}_{-16}	73413^{+17}_{-18}	73402^{+63}_{-55}
σ_J	RV Jitter (m/s)	37^{+23}_{-17}	37^{+27}_{-16}	70^{+210}_{-70}
σ_J^2	RV Jitter Variance	1420^{+2300}_{-1000}	1390^{+2800}_{-920}	5000^{+76000}_{-7100}
Transit Parameters:		LCO UT 2019-04-15 (I-band)	TESS	
σ^2	Added Variance	$0.00000202^{+0.00000030}_{-0.00000026}$	$0.0000001792^{+0.0000000063}_{-0.0000000062}$	
F_0	Baseline flux	0.99981 ± 0.00013	1.0000143 ± 0.0000053	